Journal of Sound and Vibration (1998) **217**(2), 283–296
Article No. sv981751

DYNAMIC ANALYSIS OF A MECHANICAL AIRBAG SYSTEM SENSOR

N. G. Pai, S. A. Tetzlaff and D. P. Hess

Department of Mechanical Engineering, *University of South Florida*, *Tampa*, *Florida* 33620, *U.S.A.*

(*Received* 4 *September* 1997, *and in final form* 12 *May* 1998)

All-mechanical sensors for automotive airbag systems offer a compact and low cost yet highly reliable alternative to electrical sensors. In this paper, a non-linear dynamic model is presented that was used to improve the hammer-blow immunity of an all-mechanical ball-in-tube sensor without jeopardizing its endurance performance. Hammer-blows are impacts from within an automobile to the steering wheel or inflator shell that can occur during system installation or from aggressive driving. Sensor endurance is measured by the stability of calibration after being subjected to a sustained vibration environment. Numerical simulations of the model have elucidated the dynamics and mechanisms of operation of such sensors. Experimental hammer-blow tests and endurance tests, as well as simulations of these tests, have been performed. It is found that hammer-blow immunity can be improved without compromising endurance performance when a ball-seat spring is introduced with at least a 2·0 mm allowable deflection. Results which show the effect of varying the spring stiffness, allowable deflection, and pre-load are presented.

1. INTRODUCTION

It is estimated that airbags will save over 3000 lives a year once all cars have airbag systems. However, such systems have extreme performance and reliability requirements. For example, an airbag must never deploy when it is not needed, yet it must remain absolutely ready for at least 15 years [1].

Driver side airbag systems with all-mechanical sensors are required to trigger when subjected to deceleration due to frontal collisions. These systems must also resist hammer-blows to the steering wheel and inflator shell from within an automobile. Shinto *et al*. [2] discuss the development of an air bag system with an all-mechanical ball-in-tube sensor that is integrated in the steering wheel. They indicate that the all-mechanical system is highly reliable, is more compact, and has lower production costs than most electrical air bag systems.

A ball-in-tube all-mechanical airbag system sensor is shown in Figure 1. It consists of a ball in a cylinder that rests against a lever, known as a d-shaft. The weight of the ball is balanced by the compression of a bias spring about a journal. In addition, the sensor includes two spring-loaded firing pins that are restrained by the d-shaft. The firing pins are released when the d-shaft rotates a fixed amount

0022–460X/98/420283 + 14 $30.00/0

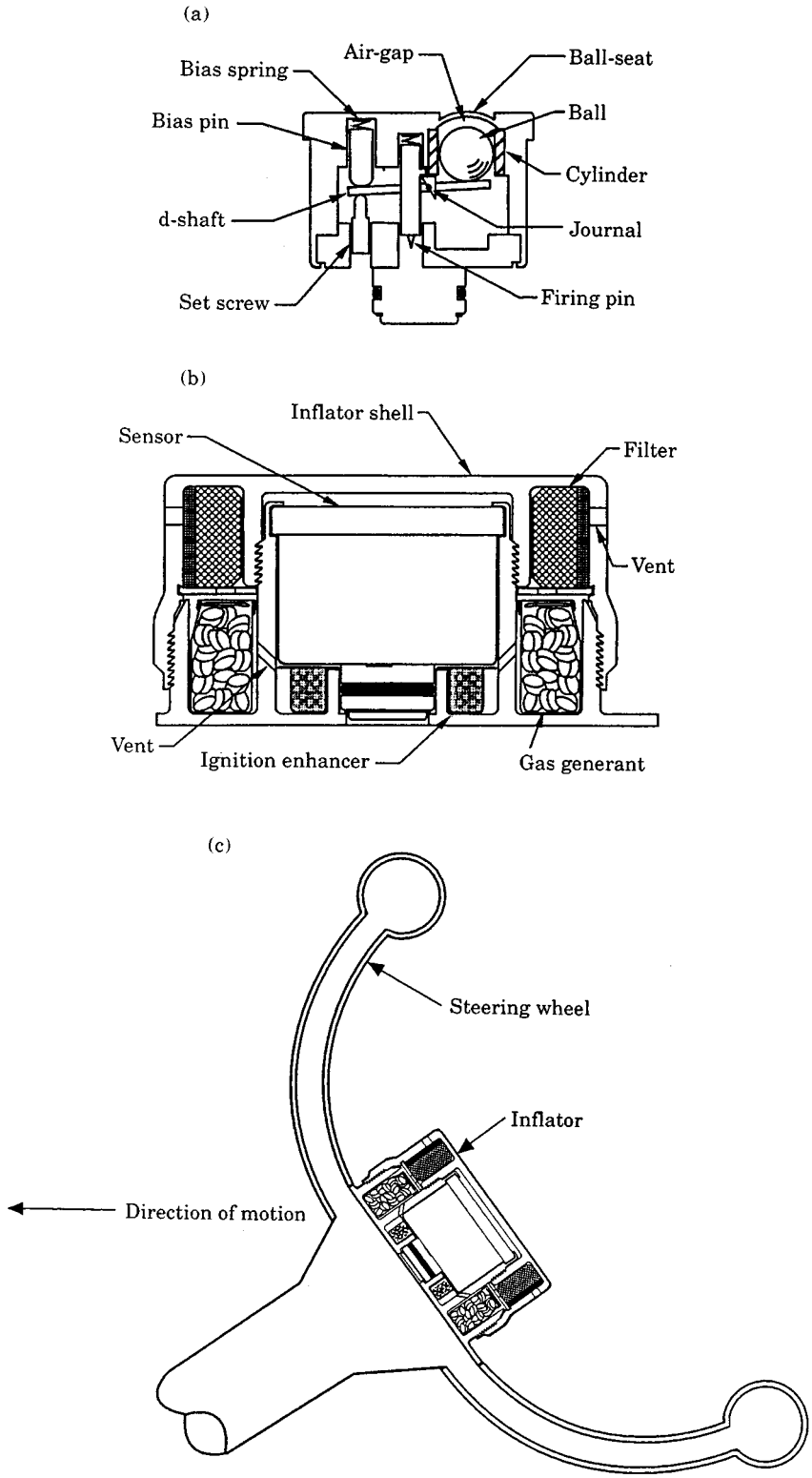

Figure 1. Typical all-mechanical ball-in-tube airbag system sensor: (a) cross-section of sensor, (b) inflator shell with sensor, and (c) steering wheel with an inflator and sensor.

about the journals. Deceleration due to frontal collision causes the ball to move forward (i.e., downward in Figure 1(a)) due to its inertia. This action rotates the d-shaft about the journals until the firing pins are released which initiates a chemical reaction within the inflator and fills the airbag. Unfortunately, other impacts to the steering wheel during or after installation can also trigger this response.

Shinto *et al*. [2] identified the bias spring and air damping as two features that suppress the sensor ball stroke when bag inflation is undesirable from hammer-blow impacts. However, improvements in hammer-blow immunity from such adjustments were found to be quite limited. A number of *ad hoc* modifications have been proposed to improve hammer-blow immunity [3]. These include: (1) adding wave washers underneath the inflator shell, (2) attaching elastomeric pads on the inflator shell, (3) including an air-gap behind the sensor ball, (4) stiffening the steering column, and (5) attaching elastomeric pads within the ball-seat. However, none of these proposed modifications, except for (3), have been implemented due to design constraints, which include space limitations, cost, and restrictions on products of combustion.

Adding an air-gap behind the sensor ball has been shown to significantly improve hammer-blow immunity [3]. However, this modification also leads to an increased shift in sensor calibration resulting from endurance tests. The shift in calibration for sensors with a 2·0 mm air-gap is about twice that of sensors without an air-gap [3]. It has been anticipated that this increase in calibration shift is due to increased wear resulting from more significant ball impacts at the d-shaft and ball-seat.

In this paper, a non-linear dynamic model of the sensor is developed and used to identify design modifications for improved hammer-blow immunity and endurance performance. It is shown that introducing a spring between the ball and ball-seat with at least a 2·0 mm allowable deflection, provides improved hammer-blow immunity without compromising endurance performance. Test results are presented which support the model simulations.

2. DYNAMIC MODEL

The dynamic model used to simulate hammer-blow impacts is shown in Figure 2. The dynamic model used to simulate the calibration process and endurance testing is shown in Figure 3. This latter model is subjected to an acceleration pulse (to simulate the calibration process) or a sinusoidal acceleration input (to simulate endurance testing), rather than force pulse, F, as used in Figure 2. A nomenclature for the parameters used in these models is provided in the Appendix. Both models accommodate planar motion of the ball, which is assumed to be a rigid body of mass m_b. The motion of the ball is defined in terms of co-ordinates x_b, y_b and θ_b. These co-ordinates are defined with respect to the configuration where the masses m_b and m_c contact spring k_{ds}, lower spring k_{bc}, and spring k_{sl} without deflection. The model in Figure 2 accommodates one-dimension of motion, defined by co-ordinate x_c, of the sensor case and the inflator shell, which are assumed to be rigidly connected with a combined mass of m_c. The model in Figure 3

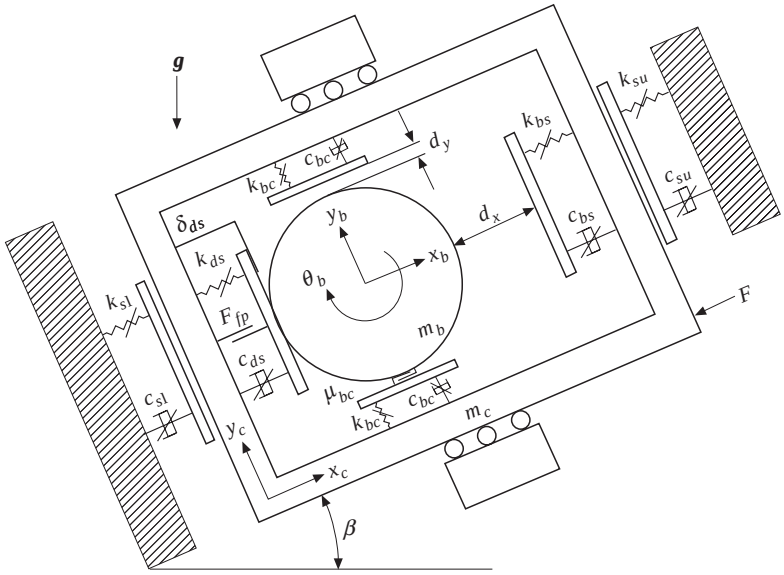

Figure 2. Dynamic model used to simulate hammer-blow impacts.

accommodates two-dimensional motion of mass m_c. This motion is defined by co-ordinates x_c and y_c, and is specified by the input acceleration. The relative displacement $(x_b - x_c)$ between the ball and cylinder is used to specify sensor triggering. Triggering is defined to occur when $(x_b - x_c) = -2{\cdot}0$ mm.

The interface between the ball and cylinder are modelled with a Hertzian stiffness k_{bc} in parallel with a Hunt and Crossley [4] type damper c_{bc}. Since all interfaces can experience contact and separation, non-linear Hunt and Crossley type dampers are used throughout. The air damping force F_a caused by the small clearance d_y between the ball and cylinder is defined in terms of the pressure

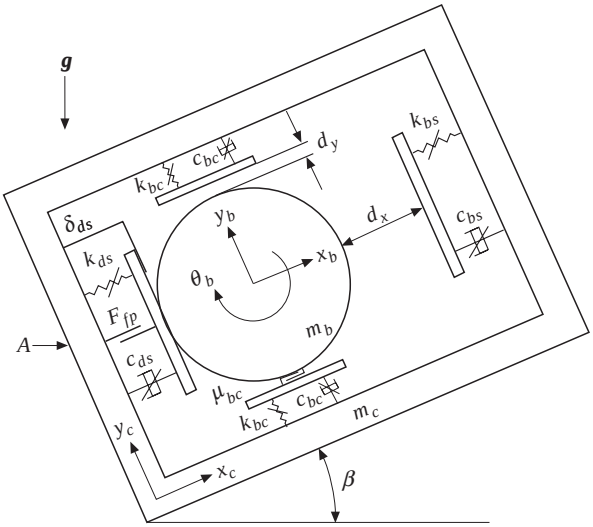

Figure 3. Dynamic model used to simulate calibration process and endurance testing.

difference on either side of the ball [5]. The friction between the ball and cylinder is modelled with a Coulomb type friction element μ_{bc}.

The ball and ball-seat interface is modeled with a Hertzian stiffness k_{bs} and damper c_{bs}. The contact between the d-shaft and ball as well as the bias spring characteristics are modelled with a spring k_{ds} and damper c_{ds}. The model also accommodates the friction force F_{fp} between the d-shaft and firing pins. Spring k_{ds} is given an initial compression δ_{ds} to model the force from the compressed bias spring in the sensor.

For the model in Figure 2, m_c is constrained to motion in the x direction. In the x direction, the motion of m_c is constrained by mounting supports, which are modelled with effective stiffness, k_{sl} and k_{su}, and damping, c_{sl} and c_{su}, elements. Note that the model allows different support stiffness in the positive and negative x directions. The equations of motion for the model in Figure 2 are

$$m_b\ddot{x}_b = -(m_b\mathbf{g}\sin\beta + F_a + F_{fc} + F_{ds} + F_{bs} + F_{ba} + F_{df}), \tag{1}$$

$$m_b\ddot{y}_b = -(m_b\mathbf{g}\cos\beta + F_{cu} + F_{cl}), \qquad I_b\ddot{\theta}_b = F_{fc}r_b, \tag{2, 3}$$

$$m_c\ddot{x}_c = (-m_c\mathbf{g}\sin\beta + F_a + F_{fc} + F_{ds} + F_{bs} + F_{ba} + F_{df} - F_{is} - F), \tag{4}$$

where the force due to air-damping is given by

$$F_a = \pi r_b^2(P_u - P_l). \tag{5}$$

The expressions used to determine the pressure difference for the air-damping force are based on an analysis by Greydanus *et al*. [5] and are

$$P_l = (m_l/V_l)RT, \qquad P_u = [(m_{tot} - m_l)/(V_{tot} - V_l)]RT, \tag{6}$$

$$V_l = \pi r_c^2(x_b - x_c), \qquad \dot{m}_l = -A_s(P_l^2 - P_u^2), \qquad A_s = 128d_y^{5/2}r_b^{1/2}/135\pi\mu RT. \tag{7}$$

The friction force between the ball and the cylinder is given by

$$F_{fc} = \mu_{bc}N_{bc}\,\mathrm{sgn}\,(\dot{x}_b - \dot{x}_c). \tag{8}$$

The normal force used to compute the friction force between the ball and cylinder is defined as

$$N_{bc} = |F_{cl} + F_{cu}|. \tag{9}$$

The force on the ball due to contact with the d-shaft is

$$F_{ds} = \mathrm{H}(x_c - x_b)(k_{ds}(x_b - x_c) + c_{ds}(\dot{x}_b - \dot{x}_c)|(x_b - x_c)|). \tag{10}$$

In equation (10), H is the Heaviside unit step function given by

$$\mathrm{H}(x) = \begin{Bmatrix} 0 & \text{if } x < 0, \\ 1 & \text{if } x \geqslant 0. \end{Bmatrix} \tag{11}$$

The force on the ball due to contact with the ball-seat is

$$F_{bs} = \mathrm{H}(x_b - x_c - d_x)(k_{bs}(x_b - x_c - d_x)^{3/2} + c_{bs}(\dot{x}_b - \dot{x}_c)|(x_b - x_c - d_x)^{3/2}|). \tag{12}$$

TABLE 1

Experimental data for friction force between d-shaft and firing pins

$x_b - x_c$ (mm)	F_{fp} (N)	$x_b - x_c$ (mm)	F_{fp} (N)
0·000	0·000	−1·143	0·157
−0·127	0·132	−1·270	0·137
−0·254	0·157	−1·377	0·113
−0·381	0·162	−1·524	0·098
−0·508	0·177	−1·651	0·083
−0·635	0·174	−1·778	0·069
−0·762	0·172	−1·905	0·059
−0·889	0·167	−2·032	0·054
−1·016	0·172	−2·159	0·069

The force on the ball due to the pre-compression of the bias-spring is given by

$$F_{ba} = -\begin{Bmatrix} \min\left((m_b \mathbf{g} \sin\beta + F_a + F_{fc} + F_{ds} + F_{bs} + F_{df}), k_{ds}\delta_{ds}\right) & \text{if } (x_b - x_c) = 0, \\ k_{ds}\delta_{ds} & \text{if } (x_b - x_c) < 0, \\ 0 & \text{if } (x_b - x_c) > 0. \end{Bmatrix} \tag{13}$$

The force on the ball due to friction between the d-shaft and the firing pin is

$$F_{df} = \mathrm{H}(x_c - x_b) F_{fp} \operatorname{sgn}(\dot{x}_b - \dot{x}_c). \tag{14}$$

The friction force on the ball due to contact between the firing pins and the d-shaft, is obtained from interpolation of the experimental data presented in Table 1. The forces on the ball, due to contact with upper and lower surfaces of the cylinder, are

$$F_{cl} = \mathrm{H}(y_c - y_b)(-k_{bc}(y_c - y_b)^{3/2} + c_{bc}(\dot{y}_b - \dot{y}_c)|(y_b - y_c)|^{3/2}), \tag{15}$$

$$F_{cu} = \mathrm{H}(y_b - y_c - d_y)(k_{bc}(y_b - y_c - d_y)^{3/2} + c_{bc}(\dot{y}_b - \dot{y}_c)|(y_b - y_c - d_y)|^{3/2}). \tag{16}$$

The force on the inflator due to contact with the support is

$$F_{is} = \begin{Bmatrix} k_{sl}x_c + c_{sl}\dot{x}_c|x_c| & \text{if } x_c \leqslant 0, \\ k_{su}x_c + c_{su}\dot{x}_c|x_c| & \text{if } x_c > 0. \end{Bmatrix} \tag{17}$$

The effect of rolling motion of the ball is incorporated into the ball velocity by adding rolling velocity $\dot{x}_{b\theta}$ defined by

$$\dot{x}_{b\theta} = \begin{Bmatrix} \dot{\theta}_b r_b & \text{if } (y_b - y_c) < 0, \\ 0 & \text{if } 0 < (y_b - y_c) < d_y, \\ -\dot{\theta}_b r_b & \text{if } (y_b - y_c) > d_y. \end{Bmatrix} \tag{18}$$

During hammer-blow tests, the inflator is subjected to a force impact. To simulate a hammer-blow, the force on the inflator due to hammer-blow impact is modelled as a half-sine pulse given by

$$F = \mathrm{H}(\tau - t)F_o \sin(\pi t/\tau). \tag{19}$$

During the calibration process, the sensor is subjected to haversine acceleration pulse of fixed amplitude, A_{co} and duration, τ:

$$A = \mathrm{H}(\tau - t)A_{co}(1 - \cos(2\pi t/\tau)). \tag{20}$$

The resulting sensor velocity at trigger, in units of miles per hour, defines the sensor calibration. For the model in Figure 3, the motion of m_c is specified by the input acceleration A. To simulate the calibration process, the motion of m_c is defined by equation (21) instead of equation (4):

$$\ddot{x}_c = \mathrm{H}(\tau - T)A_{co}(1 - \cos(2\pi t/\tau))\cos(\beta),$$
$$\ddot{y}_c = -\mathrm{H}(\tau - T)A_{co}(1 - \cos(2\pi t/\tau))\sin(\beta). \tag{21}$$

Details of the endurance test are described in section 5. To simulate endurance testing, mass m_c is subjected to sinusoidal acceleration defined by equation (22) instead of equation (4):

$$\ddot{x}_c = A_{eo}\cos(2\pi t/\tau)\cos\beta, \qquad \ddot{y}_c = -A_{eo}\cos(2\pi t/\tau)\sin\beta. \tag{22}$$

3. SIMULATIONS

The equations of motion are solved numerically using the classical fourth order Runge–Kutta method. The model parameters used for the simulations are listed in the Appendix. The values of these parameters were determined from a combination of experimental testing and analysis.

Preliminary simulations reveal that two distinct mechanisms of triggering exist for hammer-blow impact and the calibration process. As stated previously, triggering occurs when the relative displacement of the ball with respect to the case, $(x_b - x_c)$, is $-2{\cdot}0$ mm. The first mechanism of triggering occurs when the positive displacement of the case exceeds the positive displacement of the ball (see Figure 4(a)). This type of mechanism occurs during the calibration process, and the positive motion of the inflator case causes triggering. The second mechanism of triggering occurs in hammer-blow impact situations. When a hammer-blow impact is applied, the case moves in the negative x_c direction. As a result the ball impacts and rebounds off the ball-seat. The negative displacement of the ball due to impact rebound with the ball-seat causes triggering (see Figure 4(b)). Note that ball rebound occurs between 0 ms and $0{\cdot}2$ ms in Figure 4(b). With an air-gap, the ball-seat has to travel the additional distance of the air-gap, before it impacts and rebounds the ball. Hence for triggering to occur, a much larger hammer-blow is necessary.

Simulations have been performed to determine which model parameters effect sensor calibration. The velocity of the sensor case at triggering, which must be within a manufacturer specified range for calibration, resulting from an acceleration pulse is calculated and used to assess the effect of parameter changes on calibration. It is found that firing pin friction, air damping, and bias spring stiffness significantly alter the calibration characteristics. Since altering sensor calibration is undesirable, these parameters are kept constant in the hammer-blow simulations.

Simulations have been performed to assess the effect of the remaining model parameters on hammer-blow immunity. Since the goal is to develop a sensor that has nearly the same hammer-blow immunity as the sensor with an air-gap, but with improved endurance performance, the simulation results are presented in terms of a dimensionless effectiveness E_{sim} defined as

$$E_{sim} = F_{tc}/F_{agc}, \tag{23}$$

where F_{tc} is the computed hammer-blow amplitude required to cause trigger of the test sensor and F_{agc} is the computed hammer-blow amplitude required to cause trigger of sensors with 2·0 mm air-gaps. It is found that decreasing ball-seat stiffness k_{bs} and increasing air-gap d_x significantly improve hammer-blow immunity as illustrated in Figure 5. Decreasing the ball-seat stiffness and increasing the

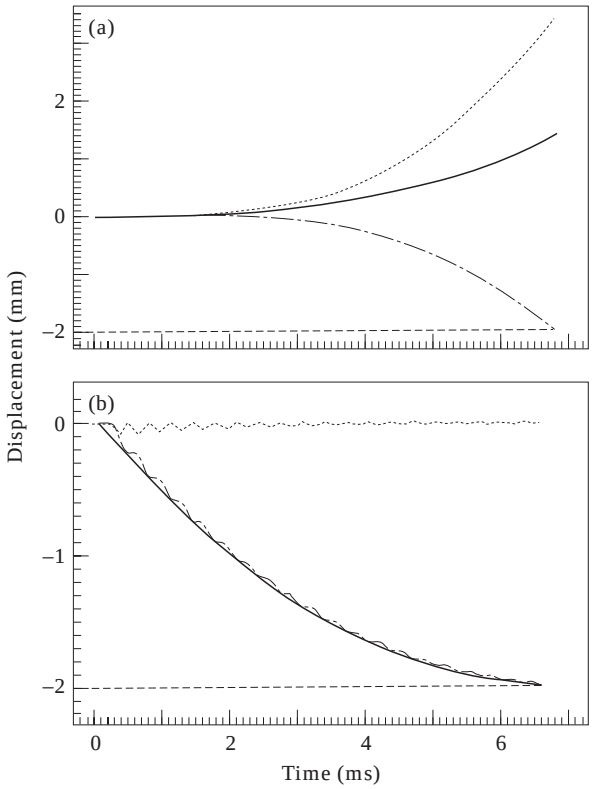

Figure 4. Simulation of two mechanism of trigger of a sensor without an air-gap: (a) during sensor calibration, and (b) due to hammer-blow impact; ——, x_b; · · · ·, x_c; —·—, $x_b - x_c$; ----, δ_t.

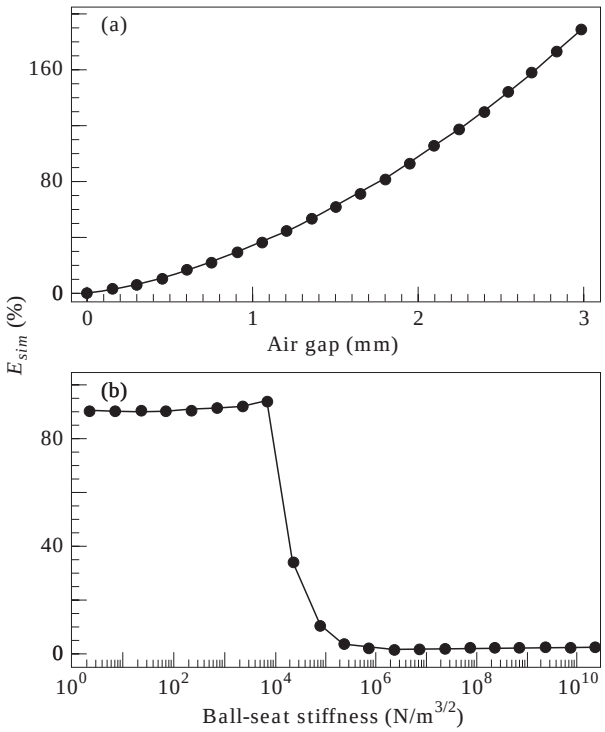

Figure 5. Hammer-blow immunity of a sensor without an air-gap as a function of (a) air-gap, and (b) ball-seat stiffness.

air-gap reduces the force transmitted to the ball during rebound F_{bs} (equation (12)), thereby reducing the level of rebound which is the cause of trigger for hammer-blow impacts. An effort to optimize the spring stiffness for a given deflection with respect to hammer-blow immunity lead to zero stiffness, which is equivalent to an air-gap. Interestingly, increasing the ball-seat damping has no significant effect on hammer-blow immunity.

Endurance test simulations have been performed to assess the effect of air-gap and ball-seat stiffness on calibration shift. As stated previously, endurance tests of sensors with an air-gap show shifts in calibration which are about twice that of sensors without an air-gap. This increase in calibration shift with air-gap is expected to be due to increased wear resulting from impacts of the ball with the d-shaft and the ball-seat. Since wear models for percussive impacts are functions of impact velocity [6], the relative velocity amplitude of the ball with respect to the case during an impact is used to assess the effect of parameter variation associated with calibration shift. Note that the sensor does not trigger during endurance tests. It is found that this relative velocity decreases when the discontinuity of the air-gap is completely removed. In addition, this relative velocity is found to decrease with increasing ball-seat stiffness. However, since low ball-seat stiffness is needed to achieve the required hammer-blow immunity, the discontinuity of the air-gap must be removed to improve endurance performance.

The removal of the air-gap and introduction of a low ball-seat stiffness can be physically implemented, without compromising any of the design constraints, by simply inserting a low stiffness spring within the existing air-gap. Such a modification introduces only minor changes in sensor assembly. Simulations of this sensor with various ball-seat spring show that acceptable hammer-blow immunity can be achieved by selecting a spring stiffness less than 10 000 N/m (refer to simulation results in Figure 5(b)) with an allowable deflection of at least 2·0 mm (see E_{sim} in Table 2). Note that to study the effect of the ball-seat spring, equation (12) was modified to accommodate the higher stiffness that occurs when the spring reaches its solid length.

Simulations also show that the endurance performance of the sensor can be improved by increasing the pre-load of the ball-seat spring to restrain the ball against the d-shaft during endurance tests. Three different helical, low stiffness, steel springs have been examined in a series of hammer-blow tests and endurance tests as described in sections 4 and 5, to assess these findings.

4. HAMMER-BLOW EXPERIMENTS

The hammer-blow test apparatus is shown in Figure 6. The apparatus consists of a 0·454 kg (16 oz) hammer head attached to a 61 cm (2 ft) bearing supported arm which is allowed to impact an inflator shell containing a test sensor. The scale provides a measurement of the angle from which the hammer is dropped. For each test, the hammer is raised from the inflator and dropped in increments of 2·5° starting at 40° until one or both of the sensor's firing pins are triggered. This trigger

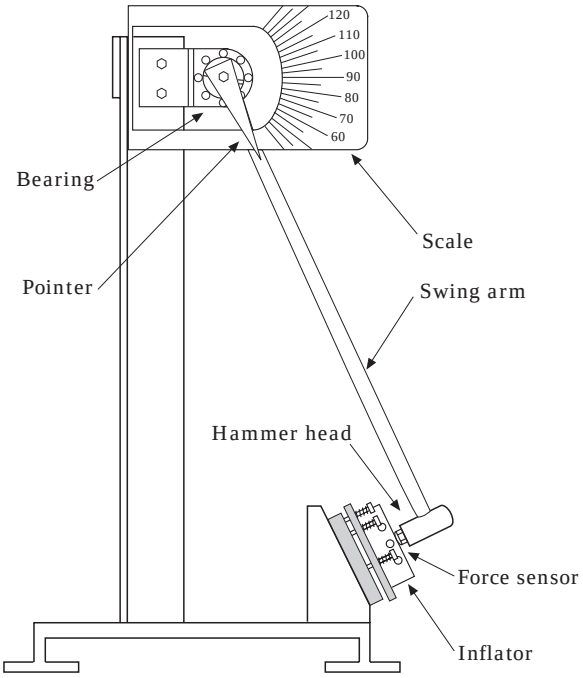

Figure 6. Hammer-blow test apparatus.

TABLE 2

Hammer-blow test results

Sensor group	Spring stiff. (N/m)	Spring pre-load (N)	Allowable defl. (mm)	E_{sim} (%)	E_{exp} (%)	Sta. dev. (%)
Air-gap	–	–	2·00	100	100	2·4
No air-gap	–	–	0·00	13	23	0·0
Spring A	100	0·33	0·70	32	64	12·7
Spring B	140	0·55	2·40	125	91	4·8
		0·62	1·90	95	90	4·0
		0·76	0·90	61	86	7·9
Spring C	210	0·24	2·25	115	92	3·3
		0·35	1·75	86	83	6·2
		0·57	0·75	35	82	8·0

angle is recorded and the test is repeated four times. In addition, the amplitude and duration of the impact force is measured and recorded with a piezoelectric force sensor. As with the simulation results, the test results are presented using a dimensionless effectiveness defined as

$$E_{exp} = F_{tm}/F_{agm}, \tag{24}$$

where F_{tm} is the measured force amplitude of the test sensor and F_{agm} is the average measured force amplitude for all test sensors with 2·0 mm air-gaps. This value can be compared to the dimensionless effectiveness calculated from model simulations as defined by equation (23).

Hammer-blow tests were performed for five different sensor types. These include sensors with a 2·0 mm air-gap, sensors without an air-gap, and sensors with low stiffness springs. Two sensors from each group were tested three times. The average effectiveness and standard deviation are computed for each sensor group and presented in Table 2. Simulation results are included in Table 2 for comparison. The data shows that the hammer-blow immunity of the sensors with low stiffness springs is comparable to that of the sensor with the air-gap, as long as the allowable spring deflection is of the order of 2·0 mm. As predicted from the model simulations, sensors without air-gaps exhibit the worst hammer-blow immunity. The results for sensors with low stiffness springs show that hammer-blow immunity improves as the allowable spring deflection increases. Although the simulation results qualitatively capture the experimental results, there are considerable differences. This difference occurs for several reasons. First, the inflator is not perfectly rigid, and hammer-blow impacts to the top of the inflator may be attenuated due to the threads, and other parts of the inflator. This results in higher hammer-blow immunity as seen in most experimental results. Also, the effective stiffness of the inserted spring may vary considerably due to shifting or misalignment of the spring within the sensor.

TABLE 3

Endurance test results

Sensor group	Spring pre-load (N)	Pulse 2 calibration shift (m.p.h.)	Pulse 2 calibration std. dev.	Pulse 4 calibration shift (m.p.h.)	Pulse 4 calibration std. dev.	Simulation impact velocity (mm/s)
Air-gap	–	0·064	0·026	0·199	0·179	145·3
Spring A	0·33	0·034	0·034	0·135	0·069	18·7
Spring C	0·35	0·038	0·017	0·198	0·045	17·4

5. ENDURANCE TEST

The endurance test subjects inflator modules with calibrated sensors to vibration in three perpendicular axes for 48 h in each direction. The inflator modules are subjected to random vibration within the frequency range of 5–500 Hz with a PSD of 0·02–0·002 $\boldsymbol{g}^2$/Hz. Three groups of sensors are subjected to the endurance tests. These include sensors with an air-gap, and sensors with two different springs inserted in the air-gap. At least five sensors from each group were tested. All sensors are tested simultaneously on the same test fixture. The calibration shift is defined as the difference between the case velocity at trigger before the endurance test and the case velocity at trigger after the endurance test. This velocity difference is defined in units of miles per hour (m.p.h.). The input for the calibration test is a haversine pulse. Two different input pulses, Pulse 2 and Pulse 4, are used. Calibration Pulse 2 is a haversine pulse of 373 m/s^2 amplitude and 10 ms duration while Pulse 4 is a haversine pulse of 133 m/s^2 amplitude and 35 ms duration. The maximum allowable calibration shifts are 0·25 m.p.h. for calibration Pulse 2 and 0·5 m.p.h. for calibration Pulse 4.

The average calibration shifts for each group are presented in Table 3. With Pulse 2, the average shifts in calibration for the sensors with springs are about half the calibration shift found for sensors with a 2·0 mm air-gap. With Pulse 4, the average shifts in calibration for the sensor group with spring A is about two-thirds the calibration shift for the other two groups of sensors. The impact velocities from model simulations are also presented in Table 3. These computed impact velocities are the ball impact velocities within the sensor obtained from endurance test simulations. These can be used to assess the amount of wear since lower impact velocities generally correlate with lower wear and correspondingly lower shifts in calibration. The relation between impact velocity, wear and calibration shift is expected to be highly non-linear. The computed impact velocities for sensors with springs are much lower than the impact velocity computed for a sensor with a 2·0 mm air-gap. In general, the sensor with lower computed impact velocities also have smaller shifts in calibration. However, the average calibration shift obtained with Pulse 4 for spring C is essentially equal to the average shift obtained for sensors with a 2·0 mm air-gap. A possible cause for this result is misalignment or buckling of spring C during endurance testing. This is expected since spring C has

an outer diameter of 4·37 mm compared to an outer diameter of 9·14 mm for spring A and 15·04 mm diameter of the sensor cylinder.

6. CONCLUSIONS

Dynamic models were used to elucidate the dynamics of an all-mechanical sensor and to propose design modifications to improve the hammer-blow immunity of an all-mechanical sensor without jeopardizing its endurance performance. Numerical simulations of the models reveal that the primary cause of hammer-blow trigger is rebound of the ball against the ball-seat. A soft spring inserted between the ball and ball-seat was found to reduce the rebound impact, and thereby increase hammer-blow immunity. A limited number of tests were performed to assess the proposed design modification. Test results show that improved endurance performance can be achieved while maintaining high hammer-blow immunity as long as the spring deflection is at least 2·0 mm. The hammer-blow tests support the simulation results in that low stiffness springs with at least 2·0 mm of allowable deflection provide acceptable hammer-blow immunity. Endurance tests results were also found to be in general agreement with the simulation results, with one exception, which was attributed to misalignment of the spring.

ACKNOWLEDGMENTS

The authors gratefully acknowledge the support of Breed Technologies of Lakeland, Florida, as well as the support from the National Science Foundation under Grant Nos. CMS-9501824 and CMS-9629217. The authors especially thank Dr. Russel Brantman and Mr. Vihang Patel of Breed Technologies for providing valuable discussions and for co-ordinating the endurance tests which were performed at Breed.

REFERENCES

1. S. Ashley 1994 *Mechanical Engineering* **116**, 58–64. Automotive safety is in the bag.
2. H. Shinto, K. Ogata, F. Teraoka and M. Fukabori 1991 *Automotive Engineering* **99**, 29–31. Simulation and testing of an all-mechanical airbag system.
3. R. Brantman 1996 Lakeland: Breed Technologies. *Private correspondence*.
4. K. H. Hunt and F. R. E. Crossley 1975 *American Society of Mechanical Engineers Journal of Applied Mechanics* **42**, 440–445. Coefficient of restitution interpreted as damping in vibroimpact.
5. J. Greydanus, M. F. Pettigrew, H. Rasmussen and J. P. G. Delaire 1995 *Mathematical Engineering in Industry* **5**, 255–267. Theoretical analysis of an airbag crash sensor.
6. R. C. Bayer 1994 *Mechanical Wear Prediction and Prevention*. Marcel-Dekker.

APPENDIX: NOMENCLATURE

A input acceleration
A_{co} amplitude of the acceleration pulse used for calibration (373·33 m/s^2)
A_{co} amplitude of the acceleration input used for endurance testing (6·43 m/s^2)

c_{bc} ball—cylinder contact damping coefficient ($4{\cdot}76 \times 10^9$ Ns/m$^{5/2}$)
c_{bs} ball—ball seat contact damping coefficient ($113{\cdot}30 \times 10^6$ Ns/m$^{5/2}$)
c_{ds} ball—d-shaft contact damping coefficient ($20{\cdot}37$ Ns/m^2)
c_{sl} inflator case—lower support contact damping coefficient ($15{\cdot}00 \times 10^6$ Ns/m^2)
c_{su} inflator case—upper support contact damping coefficient ($540{\cdot}00 \times 10^6$ Ns/m^2)
d_x air-gap in x direction ($2{\cdot}00$ mm)
d_y clearance between ball and cylinder in y direction ($0{\cdot}04$ mm)
F hammer-blow impact force
F_a air damping force
F_{ba} force on the ball due to pre-compression of the bias spring
F_{bs} force due to ball—ball-seat contact
F_{cl} force due to ball—cylinder lower contact
F_{cu} force due to ball—cylinder upper contact
F_{df} force on ball due to friction between d-shaft and firing pins
F_{ds} force due to ball—d-shaft contact
F_{fc} force due to friction between ball and cylinder
F_{fp} force on d-shaft due to friction between d-shaft and firing pins
F_{is} force due to inflator—support contact
F_o amplitude of input force
$\boldsymbol{g}$ acceleration due to gravity ($9{\cdot}81$ m/s^2)
I_b mass moment of inertia of ball
k_{bc} ball—cylinder contact stiffness ($3{\cdot}97 \times 10^{10}$ N/m$^{3/2}$)
k_{bs} ball—ball-seat contact stiffness ($2{\cdot}36 \times 10^8$ N/m$^{3/2}$)
k_{ds} ball—d-shaft contact stiffness ($135{\cdot}86$ N/m)
k_{sl} inflator case—lower support contact stiffness ($5{\cdot}5 \times 10^5$ N/m—apparatus, 5×10^7 N/m—table top)
k_{su} inflator case—upper support contact stiffness ($4{\cdot}5 \times 10^9$ N/m)
m_b ball mass ($0{\cdot}016$ kg)
m_c combined mass of sensor case and inflator case ($0{\cdot}436$ kg)
m_l mass of air on lower side of the sensor
m_{tot} total mass of air inside the sensor
N_{bc} normal force between ball and cylinder
P_l pressure acting on the ball on lower side of the sensor
P_u pressure acting on the ball on upper side of the sensor
R gas constant for air ($286{\cdot}98$ J/kg K)
r_b ball radius ($7{\cdot}50$ mm)
t time
T temperature of air inside the sensor (300 K)
V_l volume of air on lower side of the sensor
V_{tot} total volume of air inside the sensor
x_b ball displacement in x direction
$x_{b\theta}$ ball displacement in x direction due to rolling
x_c inflator case displacement in x direction
y_b ball displacement in y direction
y_c inflator case displacement in y direction
β steering column pitch (23°)
δ_{ds} initial deflection of the bias spring ($5{\cdot}20$ mm)
δ_t relative displacement of ball with respect to inflator case to cause trigger ($-2{\cdot}00$ mm)
μ dynamic viscosity of air ($1{\cdot}85 \times 10^{-5}$ Ns/m)
μ_{bc} coefficient of friction between ball and cylinder ($0{\cdot}3$)
θ_b angular displacement of the ball
τ duration of input pulse ($0{\cdot}40$ ms—hammer-blow, 10 ms—calibration pulse 2, 50 ms—endurance tests)